# Study of cleavage fracture in ferritic stainless steels. Part I: Development and characterization of model microstructures

Lucie Jacquet, Nicolas Meyer, Maximilien Libert, Frédéric de Geuser, Muriel Braccini, Rafael Estevez, Marc Mantel

# Study of cleavage fracture in ferritic stainless steels
# Part I: Development and characterization of model microstructures.

Lucie JACQUET[a,b], Nicolas MEYER[b], Maximilien LIBERT[b], Frédéric DE GEUSER[a], Muriel BRACCINI[a*], Rafael ESTEVEZ[a], Marc MANTEL[a,b]

[a] Univ. Grenoble Alpes, CNRS, Grenoble INP, SIMaP, 38000 Grenoble, France
[b] Research center, Ugitech, 73400 Ugine, France
* corresponding author : muriel.braccini@simap.grenoble-inp.fr

**Abstract:** A major drawback in ferritic steels production and usage is their mechanical brittleness at temperatures close to ambient temperature. Precipitation and grain size appear as two major parameters in such cleavage brittle behavior. This is why six model microstructures have been elaborated from the same base of chemical composition, but with different elements additions and thermal treatments. The base composition is 18% chromium and 2% molybdenum to ensure an entirely ferritic matrix at any temperature even with 0.015% of both carbon and nitrogen. The addition of titanium or niobium changed the nature, size and location of the carbides and nitrides, while carefully chosen heat treatments varied the size of the grains. Microstructure characterizations down to very fine scales (TEM, SANS) combined with thermodynamics and diffusion modeling allowed analyzing precipitates formation as well as remaining interstitial elements (carbon and nitrogen) in solution in the ferritic matrix. This multi-scale analysis of the microstructures is important to understand the mechanical behavior of the alloys, which will be presented in a companion paper.

**Keywords:** ferritic stainless steels; model microstructures; thermomechanical processing; precipitation; interstitial elements

## *1 Introduction*

Four main families of grades make up the metallurgy of stainless steels: austenitic, martensitic, ferritic and duplex stainless steels. These families are distinguished by the nature of their major constituent phases. Austenitic stainless steels, enriched with chromium and nickel, are the most widely produced (around 75% of the world market [1]), and are appreciated for their mechanical properties (high ductility and strain hardenability, high resilience at low temperature) and their resistance to corrosion [1–3]. Ferritic steels, whose chromium content varies from 11 to 30%, have lower alloying element contents than austenitic steels, and do not contain nickel or only a residual content. In addition to their generally low cost, these steels have the particularity of being ferromagnetic, a necessary asset for the design of solenoid valves, for example, used in the automotive and household appliance fields. Ferritic grades can be an alternative to austenitic ones, some of them with very good corrosion resistance: AISI 444 (EN 1.4521) ferritic grade has a PREN (Pitting Resistance Equivalent Number) equivalent to that of AISI 316 austenitic grade. The major drawback of ferritic steels is the strong dependence of their mechanical behavior on temperature which causes mechanical brittleness at low temperatures for mild steels, and at room temperature for ferritic stainless steels [4–7]. Their production and uses are then limited because of brittle fracture.

The objective of this work is to understand the mechanisms that govern cleavage brittle fracture in ferritic stainless steels and to quantify the role of two microstructural parameters of major importance: precipitation and grain size. To achieve this goal, we have elaborated different microstructures to establish relations between precipitation and grain size and fracture properties. Two consecutive articles bring together the results of this research work. This first article focuses on the characterization of these microstructures resulting from the same base of chemical composition, namely 18% chromium and 2% molybdenum to ensure an entirely ferritic matrix at any temperature. The chemical compositions will be systematically expressed

as a weight percentage. The carbon and nitrogen content is set at C + N ≈ 0.030%, which is a content accessible via current processing means with an AOD (Argon Oxygen Decarburization) [8]. The addition of titanium or niobium changes the nature, size and location of the carbides and nitrides, while carefully chosen heat treatments will vary the size of the grains to obtain six distinct microstructures. The second article brings together the mechanical characterizations (impact tests, tensile tests with smooth and notched axisymmetric specimens) and the description of the mechanisms that govern cleavage brittle fracture of the six microstructures.

During cooling, precipitation of chromium carbides and nitrides in ferritic stainless steel is due to the drastic decrease of carbon and nitrogen solubility limit in ferrite [9]. The second factor which inevitably leads to the precipitation of $Cr_2N$ nitrides and $(Cr,Fe)_{23}C_6$ carbides is the high diffusion rate of the interstitial elements in the ferritic structure. Thus, even during a hyperquenching, this precipitation cannot be avoided contrary to what is observed in austenitic stainless steels. These precipitates germinate intra or intergranularly depending on the cooling conditions: inside the grains for high cooling rates and at the grain boundaries for lower cooling rates [10]. This precipitation has an embrittlement effect [11] and causes sensitization of grain boundaries to intergranular corrosion due to local chromium depletion on either side of the grain boundary. Ductility and corrosion resistance can be restored by an annealing heat treatment between 750 and 900 °C during which the carbides and nitrides coalesce and the chromium content is homogenized in the ferrite grains [12]. The precipitation of chromium carbides and nitrides can also be avoided by adding a sufficient amount of stabilizing elements such as titanium and niobium, that have a greater affinity with carbon and nitrogen than chromium. The intragranular carbonitrides formed in this case, TiN, TiC, Nb(C,N), precipitate at a higher temperature than chromium carbides and nitrides [2,13]. Stabilization tends to limit the brittleness of ferritic grades [14] but over-stabilization can be harmful due to the precipitation of intermetallic phases [15], 16]. During the production of these steels, deoxidation and desulphurization reactions take place to avoid inclusions of oxides and sulphides. However, very low contents of these elements remain (<0.010%) and inclusions of lime silicoaluminate oxides and manganese sulphides are observed in practice.
Other phases can also form and lead to embrittlement, such as intermetallic phases of sigma, chi or alpha prime type [1,16]. However, the kinetics of formation of these phases is relatively slow in ferritic steels and these intermetallic phases are not encountered following recrystallization heat treatments or even during welding operations. They will therefore not be studied in this work.
The state of precipitation in steels stabilized with titanium and/or niobium is well described in the literature [17] : as long as the quantity of stabilizers is sufficient, all the carbon and nitrogen precipitate in the form of carbonitrides of titanium and niobium. In unstabilized grades, the chemical composition and crystallography of chromium carbides and nitrides are clearly identified, but no study indicates whether carbon and nitrogen completely precipitate in the ferritic matrix following hyperquenching. Indeed, the quantitative characterization of this fine precipitation, the size of which can be nanometric, is complex and requires heavy means of investigation.
In this first article, we explain our choices of chemical compositions and thermomechanical treatments to develop the six model microstructures for which only the precipitation and/or the size of the grains from laboratory ingots vary. We characterize the three microstructures stabilized with titanium or niobium and the three unstabilized microstructures using increasingly powerful tools to quantify grain size and study precipitation: optical microscopy (OM), scanning (SEM) and transmission (TEM) electron microscopies, small-angle neutron scattering (SANS). We will then discuss the presence or absence of carbon and nitrogen in solid solution, depending on the temperature and duration of the heat treatment and the rate of cooling of the ferrite in unstabilized grades.

## 2 Experimental methods

### 2.1 Development of the studied microstructures

To study the brittle fracture of stainless steels with a 100% ferritic matrix, the first step is to develop model materials. In order to vary only one element at a time to study its influence, we worked with laboratory casts. To ensure a ferritic structure from solidification and at any temperature, Figure 1 shows that 18% chromium is sufficient for a carbon content of 0.03%. 2% of molybdenum, an alpha-gene element, were also added to approach the chemical composition of AISI 444 industrial cast (18Cr-2Mo stabilized with Ti and Nb).

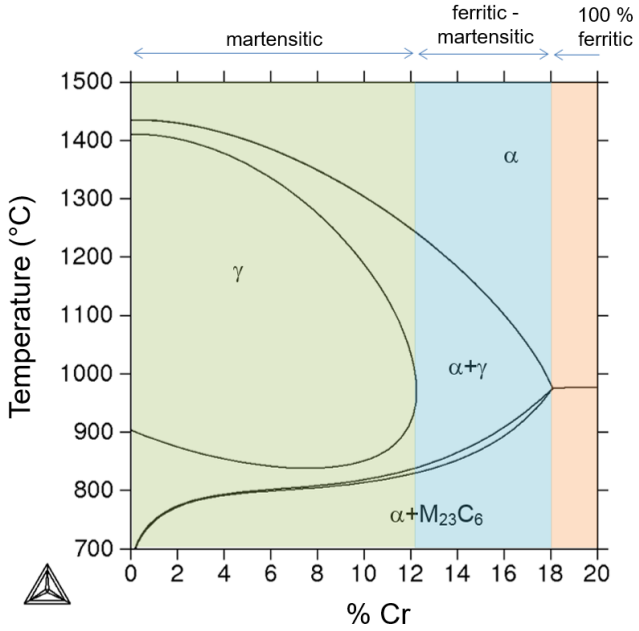


**Figure 1: Isopleth section of the Fe-xCr-0.3Si-0.3Mn-0.03C system calculated with ThermoCalc software and the TCFE6 database.**

Six microstructures were made from three different grades: one stabilized with titanium, one stabilized with niobium and the last one unstabilized. The carbon and nitrogen contents were kept constant for all the grades with a value of C + N ~ 0.030%. The Ugitech Research Center (CRU) is able to produce ingots of 25 kg of metal, with a square section of 10 x 10 cm², in a VIM (Vacuum Induction Melting) furnace. In order to produce enough metal for the study, five ingots were elaborated: Ti1 for the titanium stabilized grade, Nb1 and Nb2 for the niobium stabilized grades and Cr1 and Cr2 ingots for the unstabilized grades (Table 1). Since Nb1 and Nb2 ingots have very similar chemical compositions, they are considered as the same alloy, as well as for Cr1 and Cr2 ingots.

| Ferritic grades | Heat | Micro-structure | Si | Mn | Ni | **Cr** | **Mo** | S (ppm) | P (×10⁻³) | Al (×10⁻³) | O (ppm) | **C** (×10⁻³) | **N** (×10⁻³) | **Ti** | **Nb** |
|---|---|---|---|---|---|---|---|---|---|---|---|---|---|---|---|
| Titanium stabilized | Ti1 | *Ti* | 0.42 | 0.47 | 0.01 | **17.9** | **2.01** | 16 | 2 | 13 | 61 | **13** | **17** | **0.19** | **X** |
| Niobium stabilized | Nb1 | *Nb* | 0.52 | 0.51 | 0.01 | **18.1** | **2.02** | 17 | 3 | 18 | 93 | **14** | **17** | **X** | **0.24** |
| | Nb2 | *NbG* | 0.51 | 0.51 | 0.01 | **18.0** | **2.02** | 18 | 3 | 22 | 104 | **16** | **16** | **X** | **0.24** |
| Unstabilized | Cr1 | *Cr, Cr0* | 0.48 | 0.49 | 0.01 | **18.0** | **2.03** | 10 | 3 | 14 | 87 | **12** | **17** | **X** | **X** |
| | Cr2 | *CrP* | 0.50 | 0.50 | 0.01 | **18.0** | **2.02** | 17 | 2 | 23 | 105 | **15** | **15** | **X** | **X** |

**Table 1: Composition of laboratory casts**

The titanium and niobium contents were chosen to trap all the carbon and nitrogen, but without excess in order to avoid the presence of intermetallic compounds. The values of titanium and niobium weight percentages are given by equation (1) with $M$ the molar mass of the element

and considering that the carbides and nitrides of titanium and niobium are perfectly stoichiometric: TiN, TiC and Nb(C,N).

$$\%(Ti\ or\ Nb) = \frac{\%(C) * M(Ti\ or\ Nb)}{M(C)} + \frac{\%(N) * M(Ti\ or\ Nb)}{M(N)} \quad (1)$$

To obtain the six model microstructures, different ranges of thermomechanical treatments were performed on the alloys in order to vary and control precipitation and grain size. These ranges of thermomechanical treatments consist of forging ingots into bars, a heat treatment at 1050°C, a cold rolling step and then one or two final heat treatments; these steps are detailed below.
(i) The ingots were forged in 40 mm x 20 mm section bars in order to break the solidification structure and allow their cold rolling with a roller mill available at the CRU. Following forging, the bars were cut in half lengthwise before undergoing a first heat treatment at 1050°C for 15 minutes followed by water quenching. The purpose of this heat treatment is to reduce the structural differences between the edge and the core of the bar. Indeed, following forging, at the edge of the bar the grains are coarse and elongated while they are finer, recrystallized and equiaxed in the center. In addition, rapid cooling by water quenching limits the precipitation of chromium carbides and nitrides, dissolved back into solid solution when maintained at 1050°C for the unstabilized grade.
(ii) Following this first heat treatment, the bars were deformed by cold rolling. Between each rolling pass, the bars were a quarter turned to reduce the square section from 19x19 mm² to 12.5x12.5 mm². Obtaining a square section is necessary for machining the impact and tensile specimen. The cold deformation, at a reduction rate of approximately 50%, facilitates the recrystallization of the grains during the final heat treatments.
(iii) The final heat treatments depend on the microstructures.

- The Ti (Ti1 ingot), Nb (Nb1 ingot) and Cr (Cr1 ingot) microstructures were obtained via a recrystallization heat treatment at 1000°C for 5 minutes followed by water quenching. The thermomechanical treatment range illustrated in Figure 2(a) constitutes our reference range in order to obtain a recrystallized fine-grained microstructure.
- The NbG microstructure (Nb2 ingot) was obtained following a heat treatment in several phases: holding at 1250°C for 30 minutes to recrystallize and then grow the grains, followed by a cooling at 1000°C in 3 hours, followed by a hold for 30 minutes at 1000°C before water quenching (Figure 2(b)). The aim of this heat treatment is to obtain a homogeneous grain growth, which necessitates the dissolution of niobium carbonitrides, and then to re-precipitate the Nb(C,N) in order to obtain the same precipitation as the one in the Nb microstructure.
- The Cr0 microstructure was obtained following a final heat treatment at 1050°C for 10 minutes followed by water quenching (Figure 2(c)). As we will see later in this article, coarse chromium carbides and nitrides are present in the Cr microstructure. Maintaining the final heat treatment of the Cr0 microstructure at 1050°C avoid these coarse precipitates thanks to the complete re-solution of the chromium carbides and nitrides.
- Finally, the last microstructure, CrP, was obtained from the Cr microstructure with an additional treatment at 850°C for 2 hours followed by water quenching (Figure 2(d)). This latter heat treatment was chosen to completely precipitate carbon and nitrogen in the form of chromium carbides and nitrides.

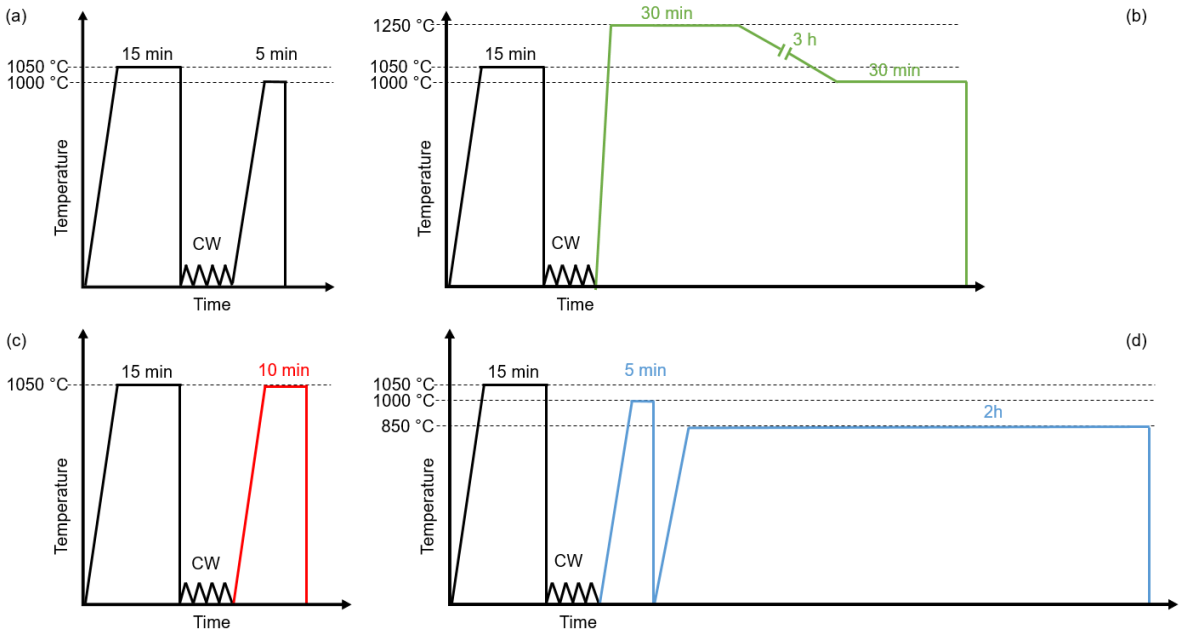


**Figure 2: Schematics of the thermomechanical treatments to obtain the six model microstructures: the Ti, Nb and Cr model microstructures (a), the NbG microstructure (b), the Cr0 microstructure (c), the CrP microstructure (d)**

Equilibrium phase diagrams obtained with the ThermoCalc software indicate the expected phases, in addition to the ferrite, for each microstructure. In the Ti microstructure, the presence of nitrides, or even carbonitrides of titanium is expected. In the Nb and NbG microstructures, only the presence of niobium carbonitrides is expected in addition to the ferrite. For the CrP microstructure, maintaining at 850°C must lead to massive precipitation of chromium carbides and nitrides, while heat treatments at 1 000°C (Cr microstructure) and at 1050°C (Cr0 microstructure) should avoid this precipitation if water quenching is effective (Figure 3). The precipitation obtained in the six microstructures will be described in the next section of the article.

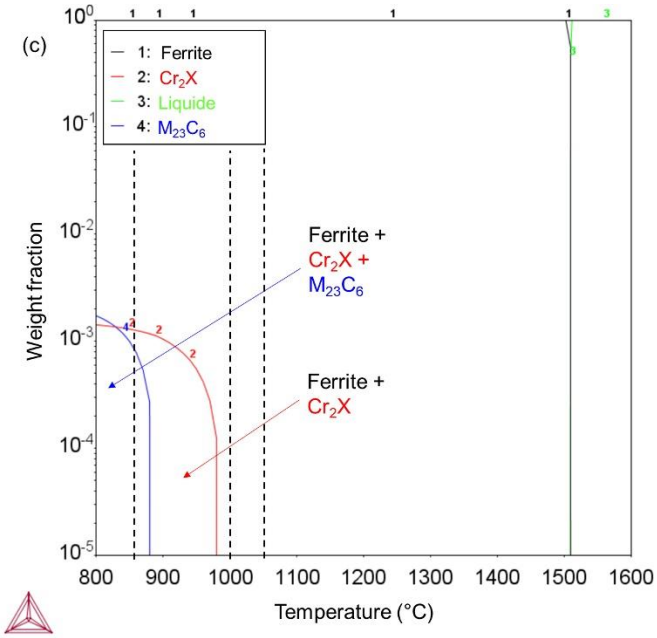


**Figure 3: Phase diagrams for unstabilized grades, with "X" of $Cr_2X$ being mostly N, obtained with the TCFE10 base from Thermo-Calc software.**

## *2.2 Tools for microstructural characterizations*

Grain size was measured by image analysis method following the ASTM E112 standard after surface polishing and color etching of the samples. For this etching, the sample is immersed for 10 to 30 seconds in a solution heated to 70°C and containing 110 ml of water, 12 ml of sulfuric acid, 4 ml of hydrofluoric acid and 5 to 6 drops of nitric acid. This etching grows an oxide film on the surface, and generates different color under polarized light according to crystal orientation. Grains which have close orientations appear in similar colors. In addition, a homogeneous color in a grain is a sign that the grain is fully recrystallized. To observe the precipitation under optical and scanning electron microscopes, the surface was prepared with Vilella etching or simple polishing. Two scanning electron microscopes were used; the SEM JEOL 7000 AF from the CRU and the SEM FEG ZEISS GeminiSEM 500 from the Consortium of Common Technological Means (CMTC) of Grenoble INP. The qualitative observation of precipitation was supplemented by EDS (Energy Dispersive X-ray Spectroscopy) analyzes. A quantitative analysis of the precipitation of the stabilized microstructures was carried out at the CRU; a large number of images were analyzed using automation of image capture and processing. Figure 4 illustrates the steps in image processing: two threshold values were set for the Nb and NbG microstructures to separate the oxides from niobium carbonitrides and a single threshold value for the Ti microstructure (because oxides are at the center of titanium carbonitrides). The nature of the particles counted is verified thanks to an EDS point analysis at the center of mass of each of them.

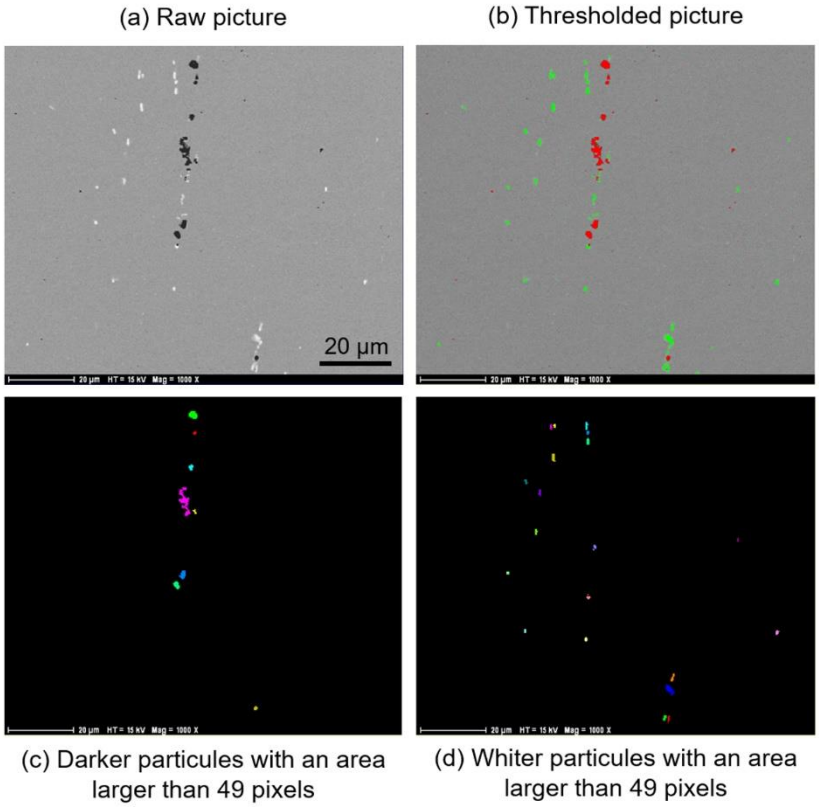


**Figure 4: Example of the automatic processing of the SEM image in backscattered electrons mode (a) to quantify size of oxides, particles darker than the matrix (c) and niobium carbonitrides, particles brighter than the matrix (d) in the Nb microstructure in the long direction.**

The conditions for acquiring the images and their processing are given in Table 2. More than 10,000 particles were quantified for each stabilized microstructure.

| Microstructure | Ti | Nb | | NbG |
|---|---|---|---|---|
| Direction | Transversal | Transversal | Rolling | Transversal |
| Magnification | 500 | 800 | 1000 | 500 |
| Number of fields | 750 | 1800 | 2504 | 750 |
| Field size (px²) | 1024 x 1024 | 1024 x 1024 | 1024 x 1024 | 1024 x 1024 |
| Analyzed area (mm²) | 42.6 | 39.9 | 35.5 | 42.6 |
| Minimum area of a particule to be counted (px) | 15 | 20 | 50 | 15 |
| Minimum area of a particule having an equivalent diameter ≥ 1µm (px) | 15 | 38 | 59 | 15 |

**Table 2: Experimental conditions for quantitative automatic SEM analyzes**

Two transmission electron microscopes were used to characterize the precipitation of unstabilized microstructures: FEG JEOL 2100F 200 keV TEM at CRU and at CMTC. Classically prepared replicas and thin sections were observed in addition to a thin section of the Cr0 microstructure prepared by FIB SEM.

Finally, the finest objects of the studied microstructures were analyzed by small angle neutron scattering (SANS) on the D11 line of the Laue Langevin Institute (ILL). 3 mm thick wafers were prepared for this purpose. The reader may refer to the work of [18] for more details on the sample preparation method and the SANS experiment. The wavelength of the neutron beam was set at $\lambda$ = 5 Å ± 0.5 Å, above the Bragg cut-off, so as to avoid any parasitic (multiple)-diffraction. Two detector-to-samples distances were used, 2.5 m and 20 m, so that the scattering vector $q$ ranged from 0.004 to 0.15 Å$^{-1}$.

A saturating magnetic field of about 1.2 T was applied by an electro-magnet, ensuring that the magnetic moment was fully aligned with the field. In these conditions, the SANS intensity collected is the sum of two components: magnetic and nuclear. Both contributions can be separated by a cos$^2$ fit of the signal along the azimuthal angle. Both the magnetic contrast signal and the nuclear contrast signal has been fitted to the same interpretation model given by the equation (2) in which the first term on the right hand side refers to a Porod behavior originating from any heterogeneity in the sample coarser than what is accessible by the q-range. The second term $L$ is a constant accounting for the incoherent contribution of the signal, which in the nuclear case is mainly due to the isotopic disorder. The third term is the contribution of the precipitates which are considered to be spherical with radius $R$ with a Schulz size distribution of width $s$ = 0.3. $f_v$ is the volume fraction of particles and $\Delta\rho$ is the scattering length density contrast (magnetic or nuclear).

$$I(q) = \left(\frac{k}{q}\right)^4 + L + f(R, s, f_v, \Delta\rho) \quad (2)$$

The volume fraction $f_v$ and the scattering length density contrast $\Delta\rho$ cannot be extracted independently from the fit of the data. In fact, in the low volume fraction limit as it is the case here, only the product $|\Delta\rho|^2 \cdot f_v$ will result from the fit of the data. Estimation of the volume fraction will then necessitate assumptions on the composition of the precipitating phases to compute the scattering length density $\Delta\rho$ as will be discussed in section 4.2.

## *3 Results*

### *3.1 Grain structure*

The grains of the six model microstructures are recrystallized and equiaxed from the edge to the center of the bar (Figure 5). The grains of the Ti, Nb, Cr and CrP microstructures have roughly the same size, with an average diameter of 70 µm. The grains in the NbG

microstructure are ten times larger than the grains in the Nb microstructure. Holding at 1250 °C for 30 minutes, followed by a slow drop in temperature to 1000 °C was effective in increasing the grain size. Note that the grains in the Cr0 microstructure are also relatively larger; their average diameter is about three times that of the grains in the Cr and CrP microstructures. Maintaining at 1050 °C for 10 minutes allowed the dissolution of the chromium carbides and nitrides, as it will be seen below, but had free the grain boundaries from their pinning.

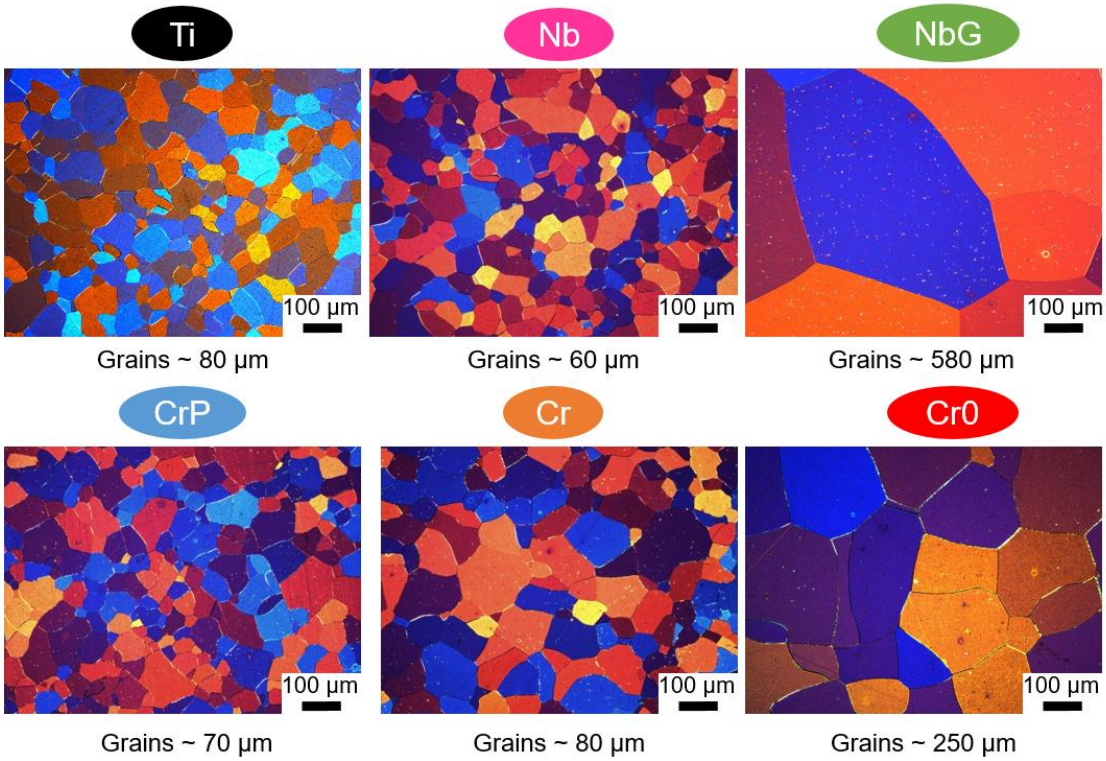


**Figure 5: Grains of the six model microstructures in transverse direction under a polarized light microscope (coloring attack).**

### *3.2 Precipitation in the stabilized microstructures*

In the Ti microstructure, particles visible at low magnification are homogeneously distributed in the ferrite grains. With SEM observation and EDS analysis, the chemical elements of these particles are identified: the nucleus is rich in Al and O while the envelope is enriched in Ti (Figure 6). Note that these particles have particular shapes, with salient angles. At higher magnification, Figure 7 reveals the outer envelope of the compounds, rich in Mo, and the presence of a fine precipitation rich in titanium distributed in the ferritic matrix. The compounds rich in Al and O are oxides that precipitate in the liquid metal and serve as nucleus sites for titanium nitrides TiN. TiN are then enveloped by titanium carbides (Ti, Mo)C that precipitated at lower temperatures.

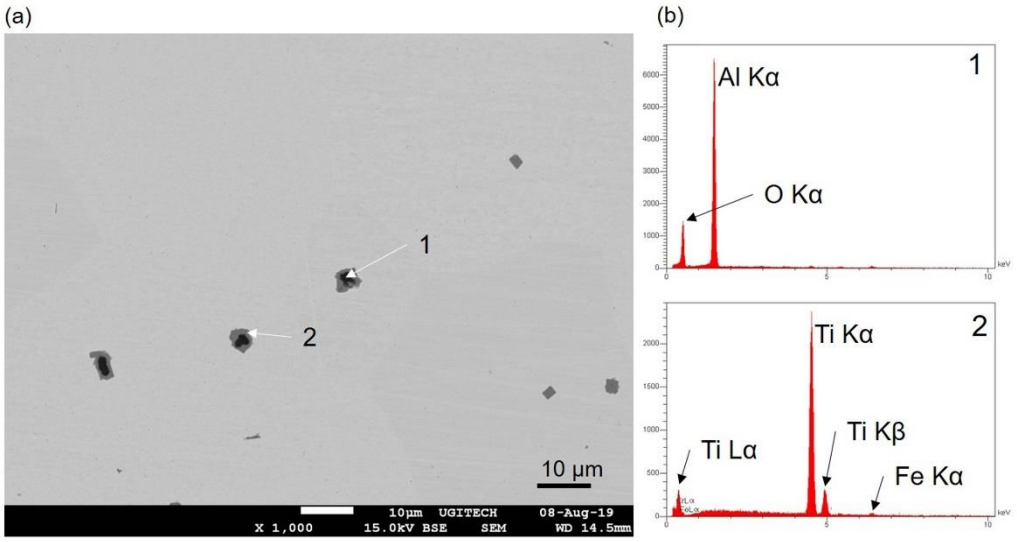


**Figure 6: Backscattered electron (BSE) mode SEM image on Ti microstructure (magnification x1000, OPS finish) (a). EDS point analyses on the two phases which constitute the complex particles (b).**

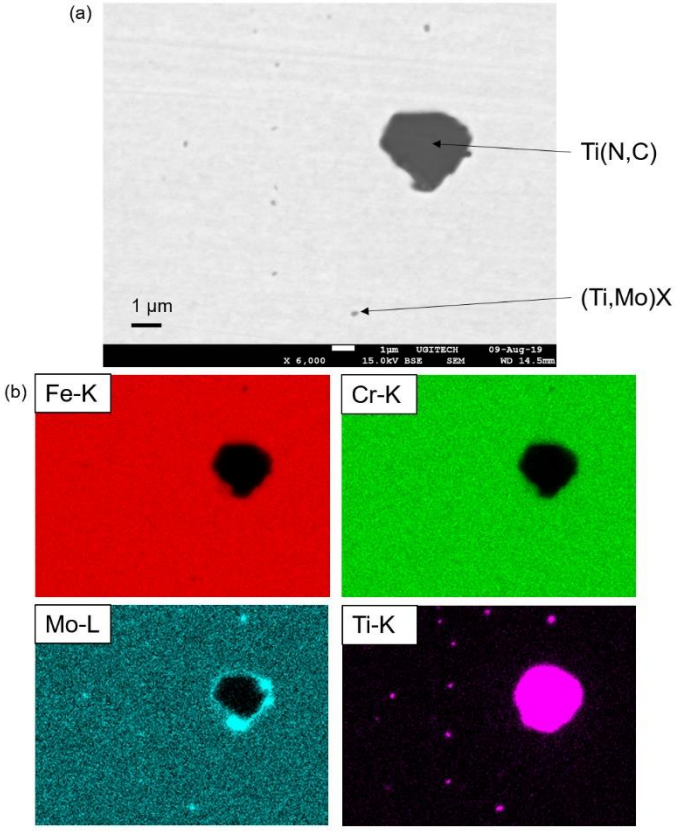


**Figure 7: Backscattered electron (BSE) mode SEM image on Ti microstructure in the long direction (a) and X ray mapping at 15 kV (simple polishing) (b). Note that the intensity scale of the spectrum corresponding to the Ti-Kα line is greatly expanded to reveal the presence of Ti in the fine particles.**

The two microstructures stabilized with niobium, Nb and NbG, present a distributed homogeneous intragranular precipitation, visible in the SEM images in Figure 8. An EDS analysis (see Figure 9) allowed to identify two types of particles: oxides, which appear darker than the matrix in the images in Figure 8, and niobium carbonitrides Nb(C, N) or (Nb,Mo)(C, N), enriched in molybdenum, brighter than the matrix. The uniformity of the silicon mapping and the absence of iron indicate that those precipitates are not $Fe_2Nb$ intermetallics but Nb(C, N), which is consistent with the low niobium overstabilization of the grades (ΔNb (Nb1) =

0.023% and ΔNb (Nb2) = 0.020%). The observed precipitation is consistent with the expected equilibrium precipitation of the phase diagram (Figure 3). It is noted that niobium carbonitrides appear to be thicker in the NbG microstructure, which will be verified in the following section.

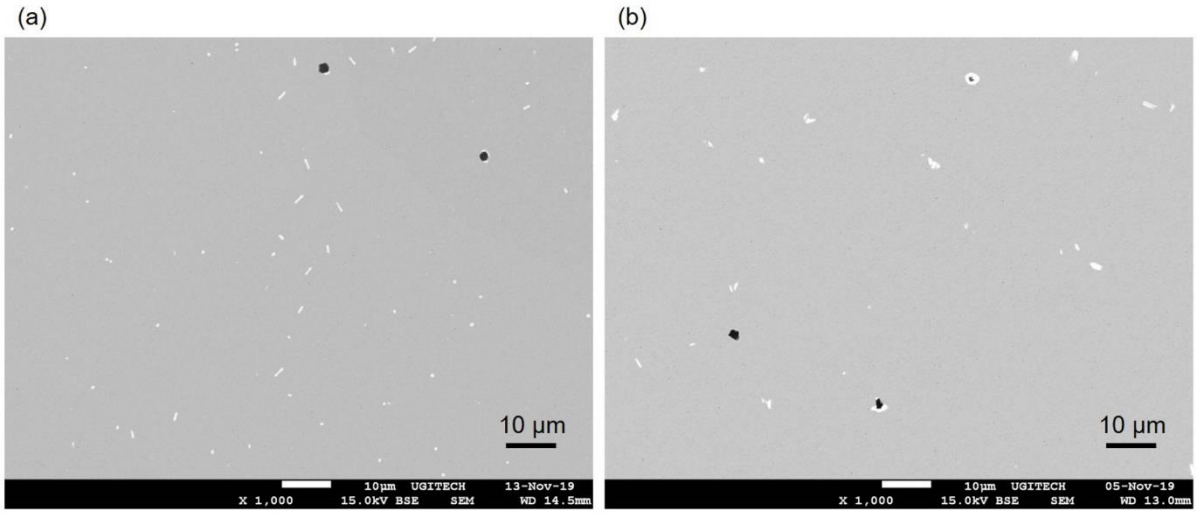


**Figure 8: Nb microstructures (a) and NbG (b) using SEM, images in backscattered mode, magnification x1000 (simple polishing).**

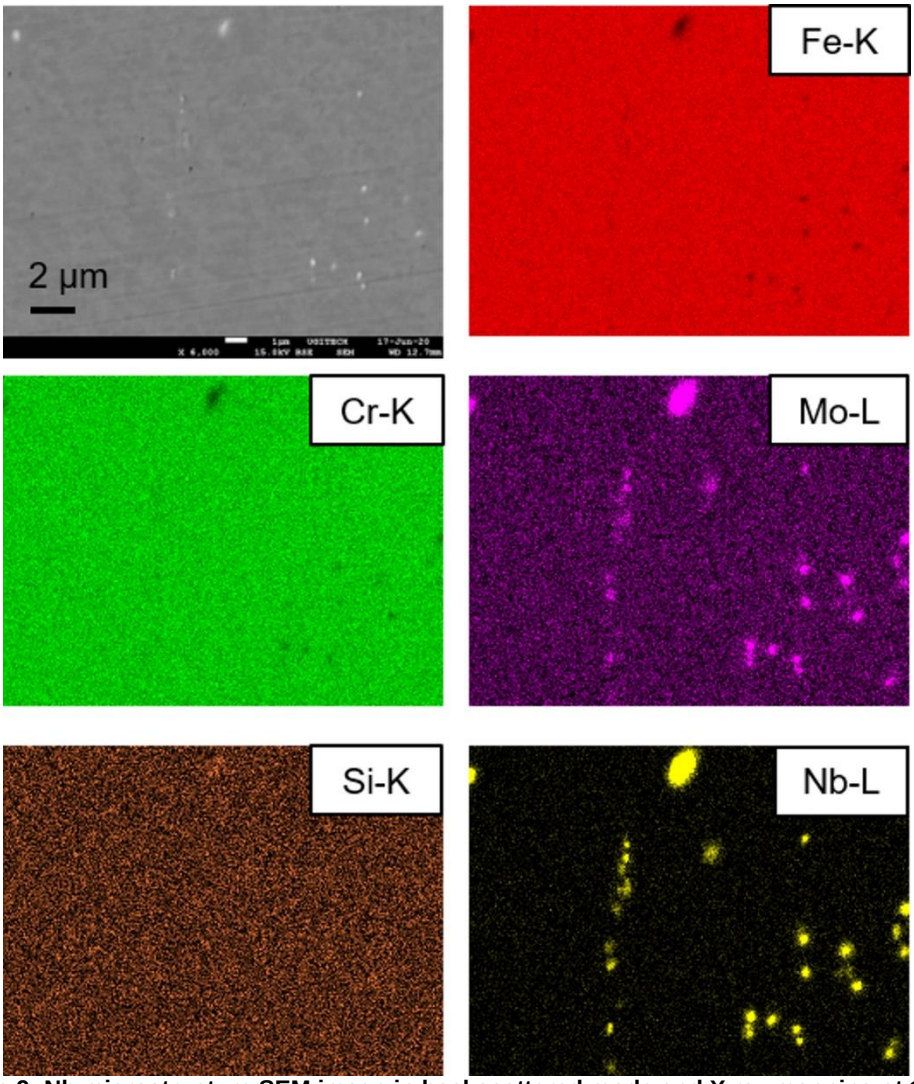


**Figure 9: Nb microstructure SEM image in backscattered mode and X ray mapping at 15 kV.**

Thanks to quantitative SEM analysis, particles size distribution is obtained using their equivalent diameter. While niobium carbonitrides and oxides can be quantified separately in the Nb and NbG microstructures, titanium nitrides and oxides are counted as a unique inclusion due to the fact that the oxides are circled by the titanium carbonitrides in the Ti microstructure. The obtained equivalent diameter histograms are given in Figure 10. Only particles with an equivalent diameter greater than or equal to 1 µm are counted.

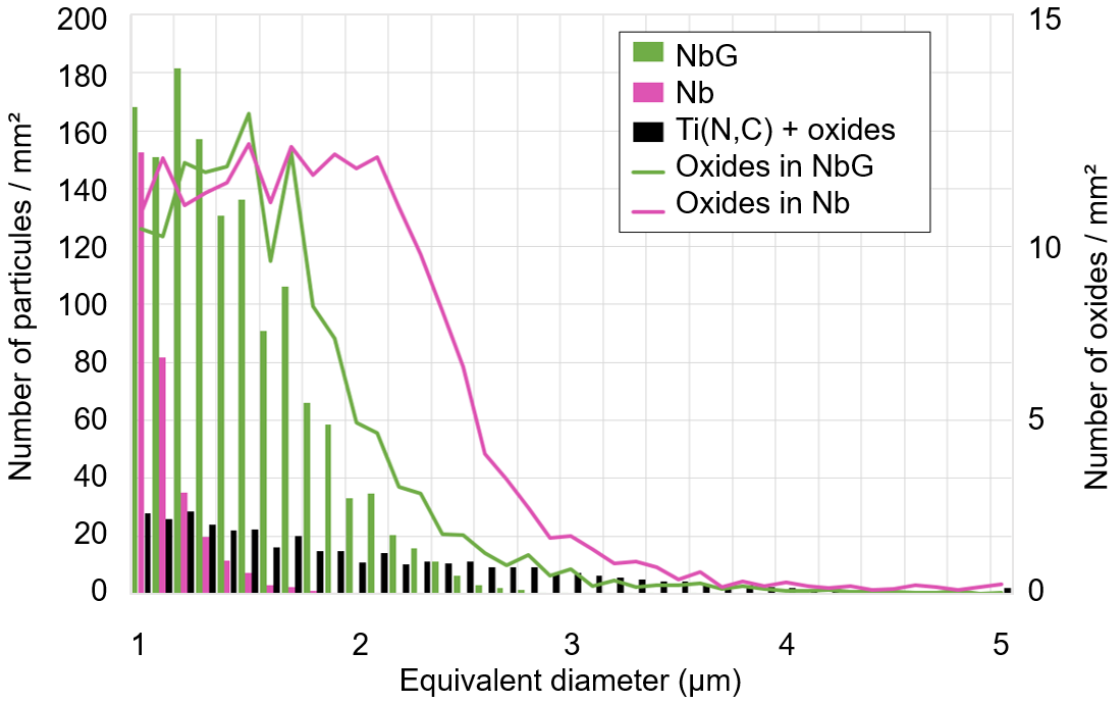


**Figure 10: Size distribution of the majority particles and of the oxides with an equivalent diameter greater than or equal to 1 µm for the Ti, Nb and NbG microstructures**

Precipitation is different in Nb and NbG microstructures: large particles are more numerous in the NbG microstructure. During the temperature rise to 1250°C, necessary to make the grains grow homogeneously, the Nb(C, N) dissolved back into solid solution but then re-precipitated during the cooling and holding at 1000°C. In the Ti microstructure, the precipitates are larger, their equivalent diameter reaching up to 4-5 µm, but they are less numerous than the niobium carbonitrides of the Nb and NbG microstructures.
Finally, in the two Nb-stabilized microstructures, we note that oxides are the largest particles present although much less numerous than the carbonitride precipitates. Indeed, the presence of oxygen between 50 and 100 ppm is inevitable in the castings despite deoxidation with aluminum and silicon. Our six model microstructures exhibit a similar population of oxides.

### *3.3 Precipitation in unstabilized microstructures*

In this part, we focus on the precipitation of the three microstructures obtained from the unstabilized grade: CrP, Cr and Cr0. Optical micrographs in figure 11 allow a first comparison of the precipitation of these three microstructures. In the CrP and Cr microstructures, intra and intergranular precipitation is observed while, at this magnification, no precipitate is visible in the Cr0 microstructure (apart from the oxides inclusions). In view of the recrystallization heat treatment of the Cr microstructure (hold at 1000°C for 5 minutes followed by water quenching), the presence of micrometric carbides and nitrides of chromium is surprising and we explain it as follows: carbides and nitrides precipitated during the rise in temperature and could not be completely dissolved back into solid solution because the holding time was too short and/or the temperature too low. For the Cr0 microstructure, with a recrystallization treatment at 1050°C for 10 minutes followed by rapid cooling by water quenching, the chromium carbides and nitrides formed during the rise in temperature were dissolved. Finally, the CrP microstructure exhibits numerous micrometric particles thanks to the precipitation heat treatment at 850°C for 2 h.

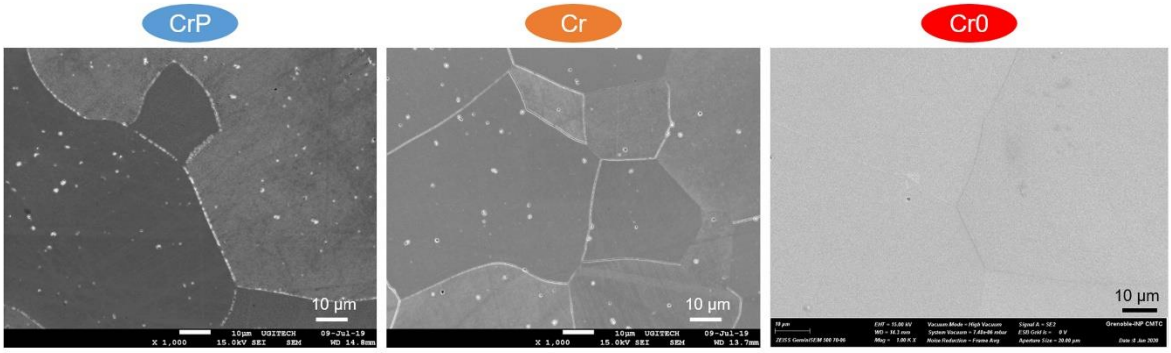


**Figure 11: Secondary electron (SE) mode SEM image of CrP, Cr and Cr0 (magnification x1000, Vilella attack).**

TEM observations confirm the presence of micrometric $M_{23}C_6$ carbides and $Cr_2X$ nitrides (being mostly $Cr_2N$) in the CrP and Cr microstructures (Figures 12(a) and (b)). In addition, $Cr_2X$ of around twenty nm are agglomerated at the grain boundaries in the Cr microstructure (Figure 12(d)). For the Cr0 microstructure, agglomerates of $Cr_2X$ precipitates (30 nm in size) are also visible at grain boundaries (Figures 12(c) and (e)), while fine intragranular precipitates, of a few nm, were identified on a thin section (Figure 12(f)).

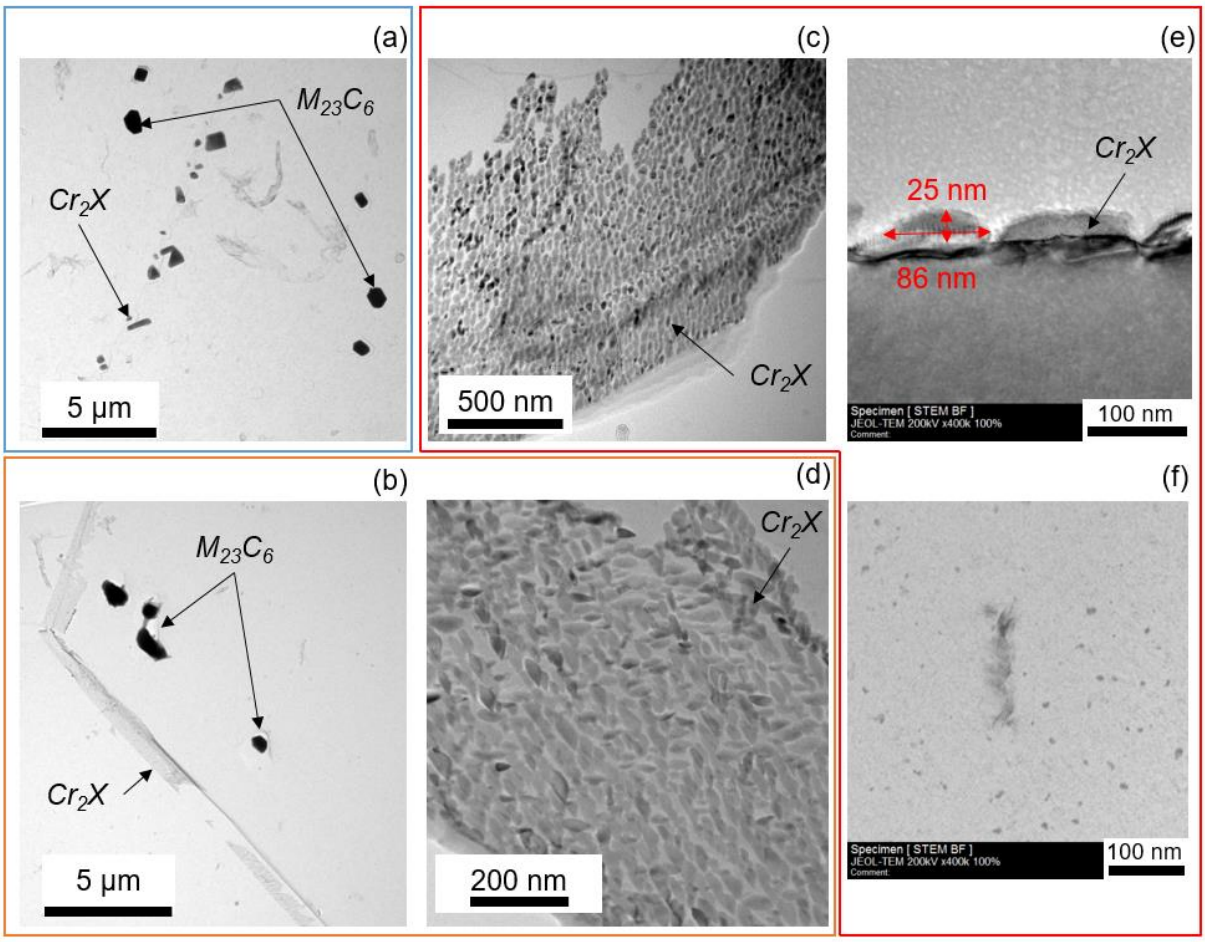


**Figure 12: TEM images on replica of CrP (a), Cr (b) and (d) and Cr0 (c) and (e). TEM image of Cr0 (f) microstructure on a thin section prepared with SEM-FIB.**

Small-angle neutron scattering (SANS) experiment at ILL complements the study of precipitation in unstabilized microstructures. In the configuration used, SANS is sensitive to objects of size between few nm to hundreds of nm. In the CrP microstructure, no precipitation

of this range of size has been detected, so that the signal consists only in the Porod and incoherent contributions. In the Cr and Cr0 microstructures, objects with a radius of around ten nm are present (Figure 13). For the Cr0 microstructure, the quantified precipitation could be the one observed with TEM on a thin intragranular section (Figure 12 (f)). The SANS data fit to equation (2) will be discussed in the next section.

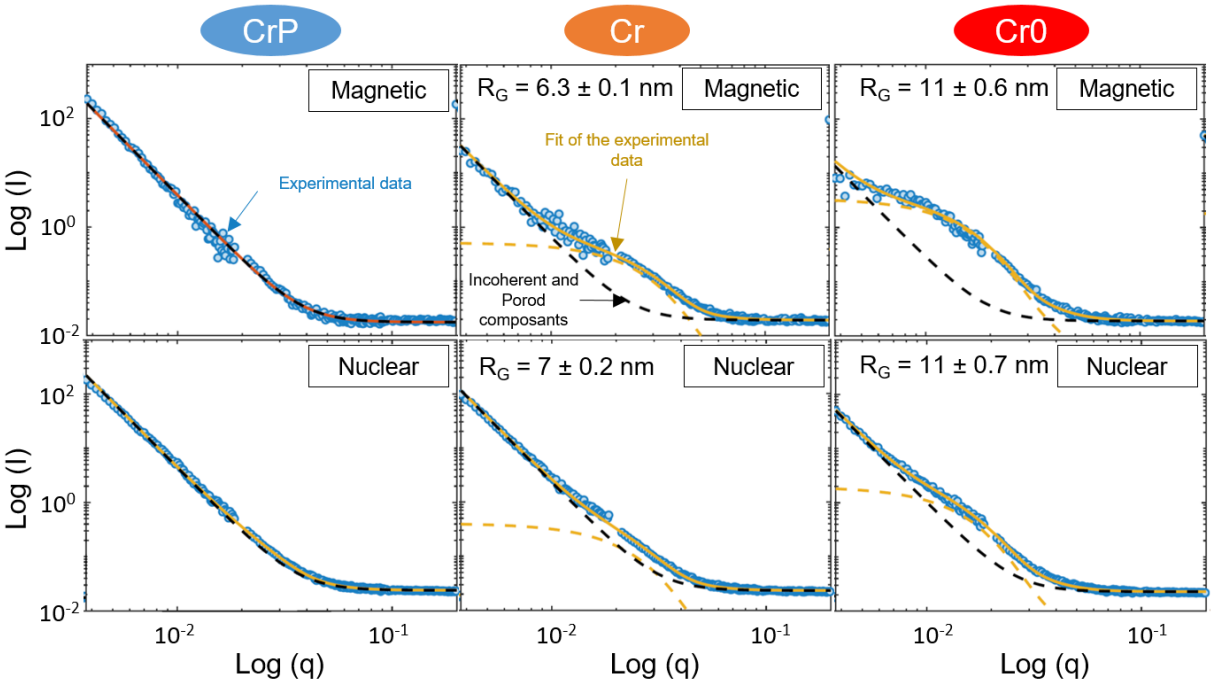


**Figure 13: Analysis of SANS data acquired on CrP, Cr and Cr0 microstructures**

## *4 Discussion*

Two of the three unstabilized microstructures, Cr and Cr0 microstructures, have been water quenched from temperatures of 1000°C or above, temperature range where C and N are completely soluble in the ferrite (Figure 14). In this part, the presence of C and N in solid solution in ferrite in those microstructures is discussed by comparing the theoretical volume fractions of precipitates to the ones measured thanks to the different methods described previously (SEM, TEM and SANS). The difference between the theoretical and measured precipitates volume fractions will help to estimate the amount of C and N in solid solution. The Cr0 microstructure is chosen as an example in the following.

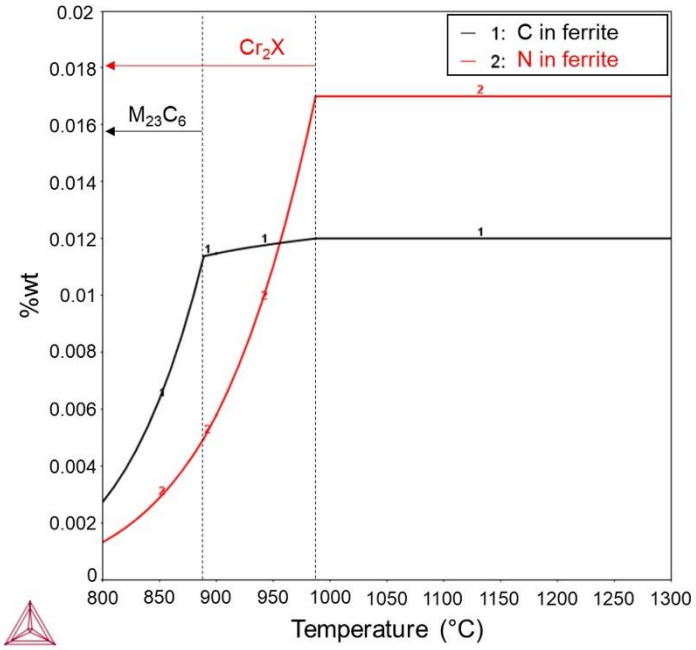


**Figure 14: Solubility limits of carbon and nitrogen in ferrite as a function of temperature for the composition of the Cr1 ingot, calculated with Thermo-Calc TCFE10 software.**

### *4.1 Theoretical volume fractions of precipitates*

Since cooling by water quenching is particularly rapid, the thermodynamic equilibrium for which $f_v^{eq}(Cr_2X) = 0.2\%$ et $f_v^{eq}(M_{23}C_6) = 0.24\%$ is certainly not reached. Figure 15 groups together the changes in the volume fractions $f_v^{meq}$ of the three types of precipitation observed as a function of temperature for the metastable equilibrium. Each volume fraction is calculated through the equilibrium between ferrite and one type of precipitate, excluding the other phases of the calculation. These fractions increase when the temperature decreases until they stabilize around 600°C, a temperature which seems to constitute an upper limit for the fraction of precipitates with:

$f_v^{meq}(Cr_2X) = 0.34\%$, $f_v^{eq}(M_{23}C_6) = 0.24\%$ and $f_v^{eq}(MX) = 0.17\%$.

We will compare these theoretical volume fractions with experimentally measured fractions.

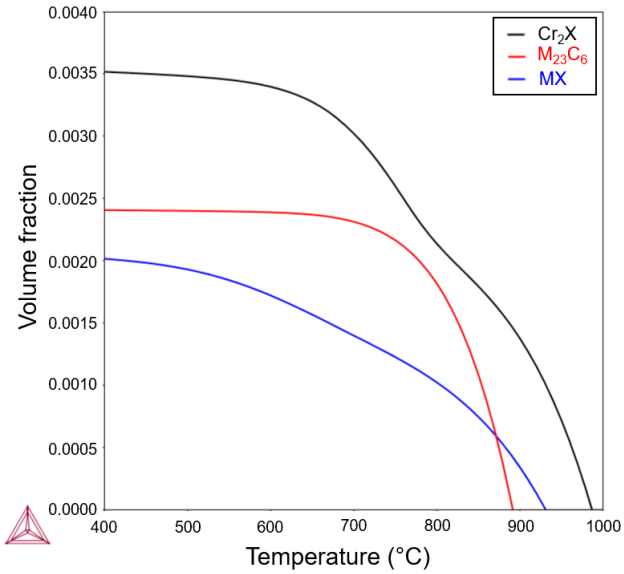


**Figure 15: Volume fraction of $Cr_2X$, $M_{23}C_6$ or MX with temperature for metastable equilibrium for the composition of the Cr1 ingot with Thermo-Calc TCFE10 software.**

## *4.2 Volume fraction of intragranular precipitates quantified with SANS*

Intra and intergranular precipitates have been identified in the Cr0 microstructure thanks to TEM observations. In addition, using SANS, a fine precipitation was quantified, but with an unknown nature and location. These may be intragranular precipitates like in Figure 12 (f), intergranular precipitates like in Figure 12 (c), or precipitates not identified by TEM. Since the intergranular precipitates are agglomerated, they would give rise to SANS signal at much lower angle than if they were isolated, and it is reasonable to assume that they would mainly contribute to the Porod contribution "baseline" so that the precipitates quantified by fitting the precipitates contribution to the SANS signal are most likely the intragranular precipitates.
Therefore, we will assume that the precipitates quantified with SANS signal are the ones observed with TEM inside the grains. Then the total volume fraction of precipitates will be the addition of the volume fraction of intergranular precipitates measured on TEM images and the volume fraction of precipitates quantified with SANS. If our assumption is wrong, then the total volume fraction of precipitates will be underestimated.

As discussed above, to estimate the volume fraction from the SANS data, the scattering length density contrast must be determined: it depends on the composition of the phases and on the origin of the contrast (nuclear or magnetic). The magnetic scattering length density has a dependence with the composition which is non-trivial [19]. It was therefore chosen to estimate the volume fraction of the precipitates from the nuclear component of the signal, for which the composition dependence of the scattering length density is potentially more discriminant.
As discussed, what is extracted from the fit is the product $|\Delta\rho|^2 \cdot f_v$. The scattering length density contrast $\Delta\rho_{nuc}$ is given by the following expression:

$$\Delta\rho_{nuc} = \rho_{nuc}^{p} - \rho_{nuc}^{m} = \frac{\overline{b_{nuc}^{p}}}{V_{at}^{p}} - \frac{\overline{b_{nuc}^{m}}}{V_{at}^{m}} \approx \frac{1}{V_{at}^{Fe}} \sum_{i} \left( c_i^{p} - c_i^{m} \right) b_i \qquad (4)$$

| | |
|---|---|
| With, $\overline{b_{nuc}^{p,m}} = \sum_i c_i\, b_i$ | Mean nuclear scattering length of precipitates ($p$) or the matrix ($m$) |
| $c_i$ | Atomic fraction of the chemical elements ($i$) |
| $b_i$ | Mean nuclear scattering length |
| $V_{at}^{p,m}$ | Mean atomic volume of the precipitates or matrix |

The nuclear diffusion length of the chemical elements of the metal is calculated from the equation $\sigma_{coh} = 4\pi\, b^2$. The coherent nuclear diffusion cross section $\sigma_{coh}$ of each chemical element is the sum of the cross sections of each of its isotopes weighted by their rate of presence. In practice, we will consider that $V_{at}^{m} \approx V_{at}^{p}$ because the precipitates and the matrix are constituted by the same atoms. The nominal composition of the matrix remains the same despite the precipitation of the particles. This assumption is valid for carbon and nitrogen because the nominal atomic composition of the matrix is already very low compared to that of the particles formed. If $c_{C,N}^{m}$ tends to 0, the difference $c_{C,N}^{p} - c_{C,N}^{m}$ will be only slightly modified. For the other chemical elements present in the precipitates, the volume fractions of precipitates will be low enough to consider that the chromium and the iron which leave the matrix to enrich these particles do not modify the average content of the matrix sufficiently to have a significant influence. The next step in the interpretation of the analysis of the data acquired with SANS requires assumptions on the composition, and therefore on the nature of the precipitation studied. The precipitates likely to be present in unstabilized ferritic grades are chromium carbides $M_{23}C_6$, chromium nitrides $Cr_2X$ or $M_2X$ and MX where M denotes iron, chromium, molybdenum, titanium and X carbon and nitrogen.

| Particules | Fe | Cr | Mo | Ti | C | N | fv Cr0 (%) |
|---|---|---|---|---|---|---|---|
| $M_{23}C_6$ | $\frac{23}{29}$x 31% | $\frac{23}{29}$x 65% | $\frac{23}{29}$x 4% | 0% | $\frac{6}{29}$x 100% | 0% | 0.032 |
| $Cr_{23}C_6$ | 0% | $\frac{23}{29}$x 100% | 0% | 0% | $\frac{6}{29}$x 100% | 0% | 0.012 |
| $M_2(C,N)$ | $\frac{2}{3}$x 13% | $\frac{2}{3}$x 87% | 0% | 0% | $\frac{1}{3}$x 50% | $\frac{1}{3}$x 50% | 0.028 |
| $Cr_2(C,N)$ | 0% | $\frac{2}{3}$x 100% | 0% | 0% | $\frac{1}{3}$x 50% | $\frac{1}{3}$x 50% | 0.02 |
| $Cr_2N$ | 0% | $\frac{2}{3}$x 100% | 0% | 0% | 0% | $\frac{1}{3}$x 100% | 0.027 |
| $MX$ | $\frac{1}{2}$x 6% | $\frac{1}{2}$x 44% | 0% | $\frac{1}{2}$x 50% | $\frac{1}{2}$x 25% | $\frac{1}{2}$x 75% | 0.05 |
| $MN$ | $\frac{1}{2}$x 6% | $\frac{1}{2}$x 44% | 0% | $\frac{1}{2}$x 50% | 0% | $\frac{1}{2}$x 100% | 0.072 |

**Table 3: Assumptions about the nature and composition of precipitation quantified by SANS and associated volume fractions, determined from nuclear contrast, in the microstructure Cr0.**

Table 3 shows the volume fractions obtained from the SANS data fitting of the scattering length density for each potential phase in the Cr0 microstructure. The iron, chromium, molybdenum and titanium contents are those measured in TEM by EDS on the observed precipitates. Since the carbon and nitrogen contents were not quantified by EDS, we estimated that there is no nitrogen in the $M_{23}C_6$ and that the carbon represents between 0 and 50% of the share of light elements in $Cr_2X$ and between 0 and 25% in MX, the rest being nitrogen. The volume fractions in Table 3 give an estimate of the actual volume fraction of the quantified precipitation.

### *4.3 Volume fraction of intergranular precipitates measured from TEM images*

The volume fraction of intergranular precipitates is estimated experimentally via TEM images before being reinforced by simulating the growth of a germ with DICTRA software. Fine precipitates agglomerated at grain boundaries are present in the Cr0 microstructure (Figures 12 (c) and (e)). The surface of these particles covers about 65% of the surface of the grain boundary. In order to estimate the volume fraction occupied by these particles the following

assumptions are made: all the grain boundaries of the Cr0 microstructure are covered by this film of particles and, a single particle on average occupies the thickness of the intergranular film.

The volume fraction of particles at grain boundaries $f_v^{pGB}$ can then be estimated using the following equation:

$$f_v^{pGB} = \frac{V^{pGB}}{V^{grain}} = \frac{S^{pGB} * e * n}{V^{grain}} = \frac{\frac{S^{grain}}{2} * f_s^{pGB} * e * n}{V^{grain}} \quad (5)$$

| | |
|---|---|
| With $V^{pGB}$ | Volume occupied by particles at grain boundaries |
| $V^{grain}$ | Average grain volume |
| $S^{pGB}$ | Surface occupied by particles at grain boundaries |
| $e$ | Average thickness of particles at grain boundaries, equal to their equivalent diameter |
| $n$ | Number of particles in the gain boundary thickness, $n = 1$ |
| $S^{grain}$ | Grain average surface |
| $f_s^{pGB}$ | Surface fraction of particles at grain boundaries |

The volume fraction of particles at the grain boundaries $f_v^{pGB}$is thus estimated at 0.02% for the Cr0 microstructure assuming the intergranular particles are cylinders.

In order to support those measurements from TEM images, thermodynamic calculations were carried out with the Thermo-Calc software and the DICTRA module (see Appendix A). First, the driving force of the two stable phases, $M_{23}C_6$ and $Cr_2X$, that may form in the unstabilized microstructures (see section 2.1, "X" being mostly nitrogen) was calculated. Those calculations have shown that the $Cr_2X$ phase is the most prone to form during cooling. Second, simulating the growth of a 1 nm thick germ at the boundary of a spherical grain during quenching, it was shown that the size of a $Cr_2X$ precipitate at the grain boundary cannot exceed about twenty nm in thickness. Those numerical results are in agreement with our experimental observations: the precipitates mainly present in the Cr0 microstructure are $Cr_2X$ and the thickness of the particles in the grain boundaries is about thirty nanometers. Finally, the corresponding volume fraction obtained from such calculations is 0.02%, in agreement with what was measured here from TEM images and ten times lower that what is predicted from thermodynamic equilibrium calculations. Thus, we can conclude that, during water quenching, the proportion of nitrogen and carbon which precipitate at the grain boundaries represents only about 10% of their nominal content.

### *4.4 Carbon and nitrogen in solid solution*

In order to determine if carbon and nitrogen remain in solid solution, Table 4 groups together the volume fractions estimated previously for the Cr0 microstructure from SANS measurements (section 4.2) as well as the intergranular precipitation volume fraction, for which the numerical calculation and the estimate from TEM image analysis gave the same value (section 4.3). Without concluding on the nature of the precipitation quantified with neutron scattering, we notice that the obtained total volume fraction is far less than the volume fraction of precipitates at metastable equilibrium, as calculated with ThermoCalc software in section 4.1.

| Intergranular precipitation (TEM) | | Precipitation quantified with the SANS | | Precipitation at metastable equilibrium at 600 °C (with Thermo-Calc) | |
|---|---|---|---|---|---|
| $Cr_2(N,C)$ | 0.02% | $Cr_2(N,C)$ | 0.02 to 0.027% | $Cr_2(N,C)$ | 0.34% |
| | | $M_{23}C_6$ | 0.012 to 0.032% | $M_{23}C_6$ | 0.24% |
| | | MX | 0.05 to 0.072% | MX | 0.17% |

**Table 4: Estimated or calculated volume fraction for microstructure Cr0**

Thus, for the Cr0 microstructure, assuming that the hypothesis made to estimate the volume fractions of particles are correct, either a precipitation containing carbon and nitrogen has not been quantified, or carbon and nitrogen remain in solid solution in supersaturation at room temperature. The difference between the expected volume fraction of precipitates and the one estimated here is at least 0.1%. Moreover, since we used increasingly sophisticated characterization tools, allowing the study of finer and finer precipitates, down to the nanometer, the precipitation of the Cr0 microstructure was particularly studied. So, we conclude that a significant amount of carbon and nitrogen remains in solid solution, from 30% to 80% of the initial amount, depending on the nature of the precipitation quantified with the neutron scattering. [21] and [11] explained that with a heat treatment to re-dissolve the chromium carbides and nitrides followed by water quenching, the grain boundaries of ferritic stainless steels are free from precipitates. The deployment and improvement of characterization tools since the publication of their articles have enabled us to conclude the opposite by observing nanometric precipitation thanks to TEM and SANS.

For the Cr microstructure, the same approach is more complex to apply because many precipitates are present in the grains with micrometric sizes for which it is difficult to give an estimate of the volume fraction (Figure 11). In this case, the sum $f_v^{pGrain} + f_v^{pGB} + f_v^{SANS}$ is of the same order of magnitude as the theoretical volume fraction determined using Thermo-Calc software with $f_v^{pGrain} \in [0.13\% ; 0.35\%]$.
Nevertheless, in the CrP microstructure, the precipitates are more numerous and larger than in the Cr microstructure. Yet, the heat treatment at 850°C, which distinguishes the CrP microstructure from the Cr, allows the precipitation of carbon and nitrogen but without prior dissolution. The precipitates observed in the CrP microstructure certainly come from the reorganization of existing precipitates (coalescence) and also from new seeds formed with carbon and nitrogen still present in solid solution before the heat treatment at 850°C. In addition, tensile tests performed at room temperature reveal that the elastic limit of the Cr microstructure is 100 MPa greater than the one of the CrP microstructure (Table 5). This difference cannot be explained by grain size effect since grain have similar size in both microstructures (Figure 5); neither by precipitation effect since precipitates are more numerous in CrP. Thus, the presence of carbon and nitrogen in supersaturated solid solution certainly justifies these differences in microstructural and mechanical properties. Moreover, we notice from Table 5 that the elastic limit of Cr0 is even higher (200 MPa greater than the elastic limit of the CrP microstructure) certainly mostly due to the presence of C and N in solid solution.

| Unstabilized microstructure | Yield strength at 25 °C |
|---|---|
| CrP | 338 ± 1 MPa |
| Cr | 450 ± 10 MPa |
| Cr0 | 539 ± 5 MPa |

**Table 5: Yield strength, determined by tensile tests at room temperature, for the three unstabilized microstructures**

## *5 Conclusions*

This first article devoted to the study of brittle fracture by cleavage in ferritic stainless steels with 18% Cr and 2% Mo focuses on the development and characterization of six model microstructures, for which the grain size, the nature and size of the precipitates and the presence of carbon and nitrogen in solid solution change.
Using two different stabilizing elements, Nb and Ti microstructures lead to comparable matrix and grain size (of about 70 µm) but with precipitates of different nature and size. In the Ti microstructure, Ti(N,C) precipitates with an angular shape and an equivalent diameter up to 4-5 µm are observed, while in the Nb microstructure Nb(C,N) precipitates are globular, smaller (equivalent diameter less than 2 µm) and more numerous. In the NbG microstructure, the precipitation is similar to the one in the Nb microstructure, even if the precipitates size is slightly larger. But the important differences between those two microstructures is the grain size, which is 10 times larger in the NbG microstructure. Thus the heat treatment consisting in a hold of 30 min at 1250°C followed by a slow cooling to 1000°C and a hold of 30 min was effective in changing the grain size while leading to a similar precipitation.
For the unstabilized microstructures, CrP and Cr microstructures have the same grain size (similar to the Nb and Ti microstructures) but the additional heat treatment at 850°C on the CrP microstructure modifies the state of precipitation. While in both microstructures $M_{23}C_6$ precipitates inside the grains and $Cr_2X$ precipitates at the grain boundaries, the precipitates are more numerous and larger in the CrP microstructure. For the Cr0 microstructure, the dissolution heat treatment at 1050°C followed by water quenching cannot avoid chromium carbides and nitrides precipitation. However, a major part of carbon and nitrogen remain in solution in the ferrite at room temperature and harden the ferritic matrix. Such an effect is also observed in the Cr microstructure but with a lesser extent.
Part II of this article will focus on the mechanical properties and brittle fracture by cleavage of these six microstructures.

### *CRediT authorship contribution statement*

**L. Jacquet**: Methodology, Experiments and Characterizations, SANS, Thermodynamic calculations, Writing-original draft. **R. Estevez**: Supervision, Writing-review&editing. **M. Braccini**: Supervision, Writing-review&editing. **F. De Geuser** : SANS **M. Libert**: Characterizations. **N. Meyer**: Methodology, Thermodynamic calculations, Funding Acquisition, Supervision. **M. Mantel**: Methodology, Supervision, Writing-review&editing, Project Administration, Funding Acquisition.

### *Declaration of Competing Interest*

The authors declare that they have no known competing financial interests or personal relationships that could have appeared to influence the work reported in this paper.

### *Data availability*

The data can be made available upon request to the corresponding author.

### *Acknowledgements*

The authors are grateful for the financial support of Ugitech and SIMaP Grenoble INP. Moreover, the authors would like to thanks all researchers and technicians of the SIMaP laboratory and the Ugitech' research center and in particular Pierre Chemelle for his help to characterize the microstructures. In addition, we would like to thanks Ralf Schweins and the rest of the staff of the ILL for their help during the SANS experiment (http://dx.doi.org/10.5291/ILL-DATA.1-01-177).

## *Appendix A. Intergranular precipitation calculations*

Thermodynamic precipitation calculations were carried out to support the measurement of intergranular precipitates volume fraction from TEM images. The Thermo-Calc software and the TCFE10 and MOBFE5 databases were used. Previous analysis of the thermodynamic equilibrium in the unstabilized microstructures reveals that $Cr_2X$ and $M_{23}C_6$ phases precipitate in the ferrite (Figure 3 in section 2.1). Then, the first step of our approach consists in calculating the driving force of each of these phases in order to determine which one has the higher probability to form. The Thermo-Calc calculation was carried out by considering three phases: ferrite, a solid solution of hexagonal structure which can describe the $Cr_2X$ phase (HCP_A3) and the $M_{23}C_6$ phase. The chemical composition was limited to the major elements, i.e. 18% chromium, 2% molybdenum, 0.017% nitrogen, 0.012% carbon, the balance being iron. It was also assumed that no segregation occurs in the grain boundaries. The results are plotted in figure A.1: the driving force obtained for $Cr_2X$ precipitation is about twice the driving force for $M_{23}C_6$. The higher the driving force, the smaller the critical radius of the nucleus and so the greater the probability of forming such a nucleus. Thus, $Cr_2X$ phase is the most prone to form precipitates (as we have observed experimentally by TEM).

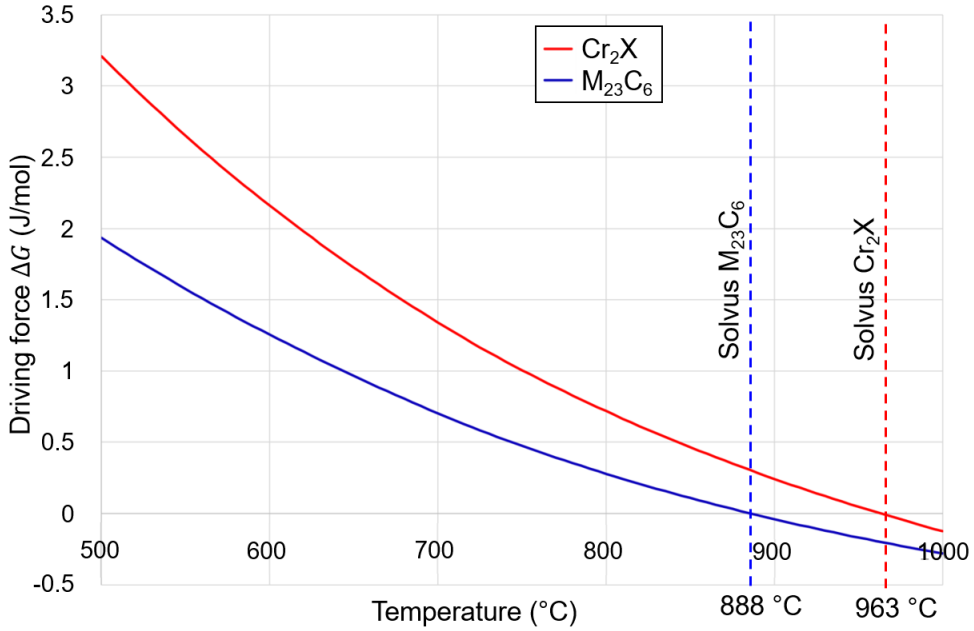


**Figure 16: Driving force for chromium carbides and nitrides precipitation as a function of temperature calculated with Thermo-Calc TCFE10**

The second step was to study the growth of a germ during the water quenching using the DICTRA module. Since $Cr_2X$ is the most likely phase to form, only the growth of this phase was considered. The DICTRA calculation were conducted with the following assumptions:

- One dimension calculations. The intergranular precipitation is described with a spherical geometry. The calculation box dimension corresponds to the mean radius of the grains and is composed of two regions: the ferritic matrix and a seed of $Cr_2X$ (phase HCP_A3#2) of thickness 1 nm which lines the sphere in order to simulate the intergranular growth of the $Cr_2X$ phase (the germ is shown in green on the diagram in Figure A.2).
- The interface between the matrix and the precipitate is of zero thickness. The composition varies discontinuously on either side of the interface.
- The interface is infinitely mobile, which means that thermodynamic equilibrium applies to the interface. This local equilibrium indicates that the compositions on either side of the interface are given by a conode of the phase diagram.

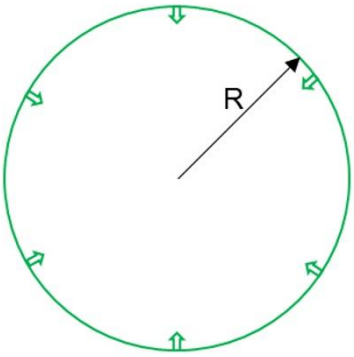


**Figure A.2: Diagram illustrating the germ from the DICTRA calculation, a film on the surface of the calculation box whose radius R is 125 µm**

The growth calculation was carried out from 1050°C down to 700°C. The starting temperature was chosen equal to the temperature of the recrystallization heat treatment applied to the Cr0 microstructure (1050 °C for 10 min). The final temperature is the temperature at which the transformation stops from a kinetic point of view. Hence, the cooling rate was estimated from the dimensions of the specimen and the abacus in Figure A.3. The thickness of the bars during the recrystallization heat treatment was 12.5 mm. Then, using the water quenching cooling curve for a part with a diameter of 10 mm can give an estimate of the cooling rate: the temperature of the part decreases from 750 °C to 100 °C in 7 seconds, corresponding to an average cooling rate of about -100 °C/s.

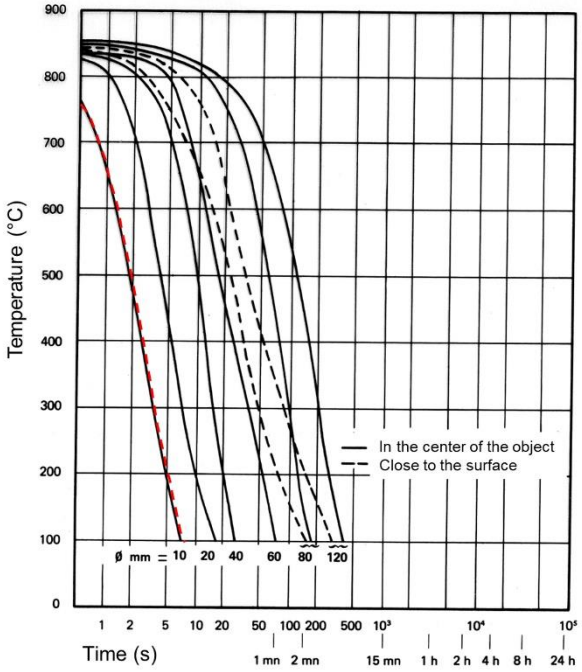


**Figure A.3: Continuous cooling curves depending on the size of the part during water quenching** [20]**.**

Finally, the chemical composition of the Cr1 ingot was simplified to the elements of primary importance in the $Cr_2X$ precipitation. Two calculations were conducted: one with a mother phase of uniform composition with 18% chromium, 2% of molybdenum, 0.017% nitrogen and the balance of iron (composition N); and one with a mother phase of composition 18% chromium, 2% molybdenum, 0.017% nitrogen, 0.012% carbon and the balance in iron (composition N+C). The obtained evolution of the germ during cooling is given in Figure A.4 as a plot of germ thickness versus temperature. It is noted that the growth begins only at 960°C, temperature from which the precipitation of the $Cr_2X$ phase becomes stable. From around 750°C, the thickness of the precipitates remains more or less constant because the

precipitation is gradually limited by diffusion at lower temperatures. The calculation can therefore be stopped à 700°C.

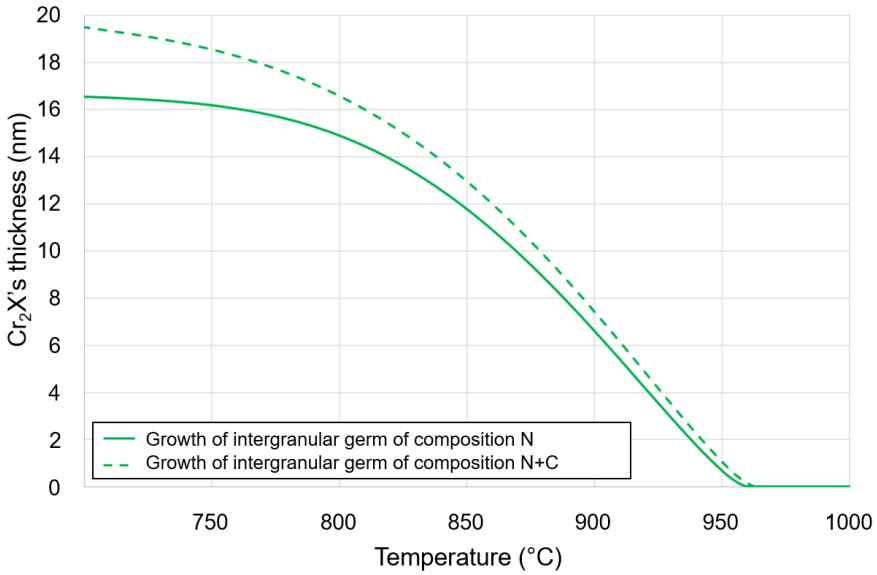


**Figure A.4: Thickness of the germ during cooling on either side of the grain boundary.**

At grain boundary, the film thickness predicted by the diffusive growth model is 17 nm with composition N, and almost 20 nm with composition N + C, assuming that the film grows on either side of the grain boundaries. The addition of carbon only slightly modifies the thickness of the precipitation because the X of $Cr_2X$ mainly denotes nitrogen (there is about 4 times more nitrogen than carbon in $Cr_2X$ at 800°C based on the metastable equilibrium calculation). These dimensions are close to the mean diameter of 30 nm of the intergranular particles measured experimentally with TEM for the Cr0 microstructure.

Figure A.5 shows the evolution of the volume fraction of $Cr_2N$ at the grain boundaries as a function of the temperature during water quenching. By comparison with the expected volume fraction if the thermodynamic equilibrium is respected, it is noted that the growth of an intergranular germ can only capture 10% of the nitrogen present in solid solution during the water quenching. A volume fraction hardly greater would be expected for the N + C composition. This result is in agreement with our experimental observations presented in section 4.3: $Cr_2X$ precipitates at the grain boundaries represent a volume fraction of 0.02% only, ten times lower than the one expected from thermodynamic equilibrium calculations.

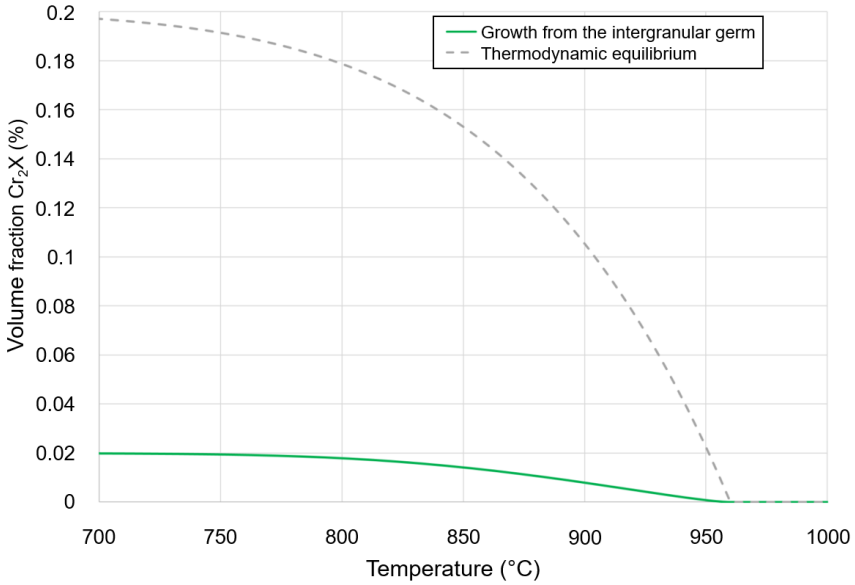


**Figure 17: Estimation of the volume fraction of $Cr_2N$ during cooling by water quenching with a growth of the germ in intergranular conditions, calculation with the composition N. Comparison with the volume fraction of $Cr_2N$ at equilibrium.**

## *References*


[1] P.-J. Cunat, J. Charles, L'acier inoxydable, d'un siècle à l'autre, La Rev. Métallurgie. 101 (2004) 971–986. https://doi.org/https://doi.org/10.1051/metal:2004182.

[2] B. Baroux, Les aciers inoxydables ferritiques à 17%Cr, in: Les Aciers Inox., Les éditions de physique, 1990: pp. 519–549.

[3] M. Durand-Charre, La microstructure des aciers et des fontes, Springer, 2003.

[4] B. Tanguy, Modélisation de l'essai charpy par l'approche locale de la rupture : application au cas de l'acier 16MND5 dans le domaine de transition, Thèse de doctorat Ecole des Mines de Paris, 2004.

[5] F. Tioguem, M. Maziere, F. Tankoua, A. Galtier, Identification of ductile to brittle transition temperature by using plane strain specimen in tensile test and correlation with instrumented Charpy impact test : experimental and numerical study, 107 (2018).

[6] H. Godin, J.-D. Mithieux, C. Parrens, G. Badinier, M. Sennour, A.-F. Gourgues-Lorenzon, Effects of cooling path and resulting microstructure on the impact toughness of a hot stamping martensitic stainless steel, Mater. Sci. Eng. A. 742 (2019) 597–607. https://doi.org/10.1016/j.msea.2018.11.036.

[7] F.M. Beremin, A local criterion for cleavage fracture of a nuclear pressure vessel steel, Metall. Trans. A. 14 (1983) 2277–2287. https://doi.org/10.1007/BF02663302.

[8] J. Saleil, M. Mantel, J. Le Coze, La production des aciers inoxydables Histoire de son développement et des procédés de fabrication. Partie II. Évolutions de l'élaboration des aciers inoxydables au four électrique à arc., Matériaux Tech. 108 (2020) 104. https://doi.org/10.1051/mattech/2020017.

[9] B.C. De Cooman, Lectures on Stainless Steel, in: Grad. Institue Ferr. Technol., 2016. https://doi.org/https://www.researchgate.net/publication/301692426_Lectures_on_Stainless_Steel_8.

[10] M. Sarkari Khorrami, M.A. Mostafaei, H. Pouraliakbar, A.H. Kokabi, Study on

microstructure and mechanical characteristics of low-carbon steel and ferritic stainless steel joints, Mater. Sci. Eng. A. 608 (2014) 35–45. https://doi.org/10.1016/j.msea.2014.04.065.
[11] H. Abo, T. Nakazawa, S. Takemura, M. Onoyama, H. Ogawa, H. Okada, The role of carbon and nitrogen on the toughness and intergranular corrosion of ferritic stainless steels, Stainl. Steel '77. (1977) 35–47.
[12] H. Sassoulas, Traitements thermiques des aciers inoxydables, Tech. l'ingénieur. ASTM M 115 (1997). https://doi.org/10.1051/metal/191007070489.
[13] A. Ostrowski, E.W. Langer, Precipitation of titanium carbonitrides in as-cast 17% chromium stainless steels, Scand. J. Metall. 8 (1979) 153–160.
[14] J.D. Redmond, Toughness of 18Cr-2Mo stainless steel, Toughness Ferritic Stainl. Steels. (1980) 123–144.
[15] M. Mantel, Baroux, Ragot, P. Chemelle, Relation entre la microstructure et la résistance au fluage et à l'oxydation d'aciers à 17% de chrome stabilisés par du zirconium et du niobium, Mémoire Études Sci. Rev. Métallurgie. (1990) 637–648.
[16] M.P. Sello, W.E. Stumpf, Laves phase embrittlement of the ferritic stainless steel type AISI 441, Mater. Sci. Eng. A. 527 (2010) 5194–5202. https://doi.org/10.1016/j.msea.2010.04.058.
[17] P. Chemelle, D. Henriet, Mise en solution et précipitation des carbonitrures de Titane et de Niobium dans les aciers ferritiques stabilisés, 1984.
[18] F. Perrard, A. Deschamps, F. Bley, P. Donnadieu, P. Maugis, A small-angle neutron scattering study of fine-scale NbC precipitation kinetics in the α-Fe-Nb-C system, J. Appl. Crystallogr. 39 (2006) 473–482. https://doi.org/10.1107/S002188980601301X.
[19] O. Tissot, C. Pareige, M.H. Mathon, M. Roussel, E. Meslin, B. Décamps, J. Henry, Comparison between SANS and APT measurements in a thermally aged Fe-19 at.%Cr alloy, Mater. Charact. 151 (2019) 332–341. https://doi.org/10.1016/j.matchar.2019.03.027.
[20] IRSID, Atlas des courbes de transformation des aciers de fabrication française, 1974.
[21] A.C.T.M. Van Zwieten, J.H. Bulloch, Some considerations on the toughness properties of ferritic stainless steels-A brief review, Int. J. Press. Vessel. Pip. 56 (1993) 1–31. https://doi.org/10.1016/0308-0161(93)90114-9.